High-pressure phase of brucite stable at Earth's mantle transition zone and lower mantle conditions

High-pressure phase of brucite stable at Earth's mantle transition zone and lower mantle conditions

Andreas Hermann[a*], and Mainak Mookherjee[b]

[a]*School of Physics and Astronomy, James Clerk Maxwell Building, The University of Edinburgh, Edinburgh, EH9 3FD, United Kingdom,* [b]*Earth, Ocean and Atmospheric Sciences, Florida State University, Tallahassee, FL, 32310, USA*

Submitted to Proceedings of the National Academy of Sciences of the United States of America

We investigate the high-pressure phase diagram of the hydrous mineral brucite, $Mg(OH)_2$, using structure search algorithms and *ab initio* simulations. We predict a new high-pressure phase stable at pressure and temperature conditions found in cold subducting slabs in Earth's mantle transition zone and lower mantle. This implies that brucite can play a much more important role in water transport and storage in Earth's interior than hitherto thought. The predicted high-pressure phase, stable in calculations between 20-35 GPa and up to 800 K, features MgO_6 octahedral units arranged in the anatase-TiO_2 structure. This suggests that brucite will transform from a layered to a compact three-dimensional network structure before eventual decomposition into periclase and ice. We show that the new phase has unique spectroscopic fingerprints that should allow for straightforward detection in experiments. The new phase also has distinct elastic properties that might make its direct detection in the deep Earth with geophysical methods possible.

brucite | pressure | phase transition | electronic structure calculations

Introduction

Water plays an important role in sustaining geological activity. For instance, water helps in lowering the mantle's melting temperature, enhancing diffusion and creep thus affecting rheology of rocks, and also influences mineral phase boundaries. Current estimates suggest that the Earth's mantle is likely to contain a mass of water equivalent to the mass of the world's oceans.(1, 2) The exchange of water between the surface and deep mantle reservoirs is vital for the sustenance of surface water over geological time scales.(3) Hydrous minerals stable in the hydrated oceanic crust and mantle play an important role in transporting water into the Earth's interior. Hydrated peridotite, the major mantle rock type, can be understood by considering mineral phases stable in the ternary system of MgO-SiO_2-H_2O (MSH). Brucite, $Mg(OH)_2$, is arguably the simplest hydrous mineral in the MSH system. Brucite is also the most important MgO-H_2O binary and the most water-rich phase within the MSH ternary system.

The crystal structure of brucite consists of Mg^{2+} cations and OH^- anions arranged in layers, in an overall trigonal structure (space group symmetry $P\bar{3}m1$), see Figure 1. The common ionic compound CdI_2 is the archetype crystal structure for brucite as well as for portlandite ($Ca(OH)_2$) and several other transition metal hydroxides $M(OH)_2$ where M= Mn, Ni, Co, Fe, Cd etc.(4–10) In brucite, the crystal structure comprises layers of edge-sharing MgO_6 polyhedra. The interaction between the layers is weak at ambient conditions, where each upward pointing OH group is surrounded by three downward pointing OH groups in the adjacent layer and vice-versa. Under compression the H—H repulsive interactions lead to positional disordering of the protons, which are displaced from the *2d* Wyckoff site into one of three equivalent *6i* sites as documented from neutron diffraction studies.(11, 12) Vibrational spectroscopic studies including infrared and Raman spectroscopy show a broad ν_{OH} stretching band with appearance of additional bands upon compression. The appearance of additional bands hints at the pressure induced frustrations of the proton.(13, 14) First principles molecular dynamics simulations also demonstrated the proton frustrations in brucite and portlandite at high pressure.(15) A first principles study at static conditions indicated that the pressure-induced hydrogen bonding in brucite is weak or unlikely to occur within the thermodynamic stability field of brucite.(16) In addition, the study also predicted that upon compression, protons may transition from a dynamic positional disorder to a static positional disorder, leading to a lowering of the trigonal symmetry to $P\bar{3}$.

Layered structures similar to that of brucite are also common in group-I (alkali) hydroxides. Under pressure, the alkali hydroxides tend not only to form hydrogen bonds between the layers, but undergo transitions to three-dimensional network structures, with 0-, 1-, or 2-dimensional hydrogen bonded sublattices.(17–20) The rationale from the high-pressure behavior of those systems is that layered phases are ultimately too loosely packed to survive under pressure. The important question relevant for deep Earth geophysics is whether brucite will undergo a similar transition and densification at high pressures, and significantly deviate from a layered structure, before decomposition into MgO and H_2O occurs. The presence of such a phase would have a significant impact on whether brucite itself could be stable in the mantle transition zone and lower mantle (potentially with quite different properties than those of the known phase), as well as the relative stability of competing MSH phases. We address this question here using structure prediction methods and first-principles total energy calculations, which enable us to bypass potential difficulties in high-pressure experiments such as sample preparation or kinetic reaction barriers. In recent years, such calculations have been crucial in making important predictions of high-pressure phases relevant for solid Earth geophysics.(21, 22) These have been very

Significance

Hydrous minerals help transporting water deep into Earth's mantle, and form part of a cycle that regulates the sustained presence of surface water on Earth. To understand the deep water cycle, it is crucial to study the properties of hydrous minerals under the conditions present in Earth's mantle. Brucite is one of the simplest hydrous minerals and stores significant amounts of water as hydroxyl groups. It is assumed to decompose in the mantle transition zone, but we show here that a more compact high-pressure phase is stabilized instead that pushes the stability region of brucite into the lower mantle. Brucite might be present in much larger quantities, and play a larger role in water transport and storage, than previously thought.

Reserved for Publication Footnotes

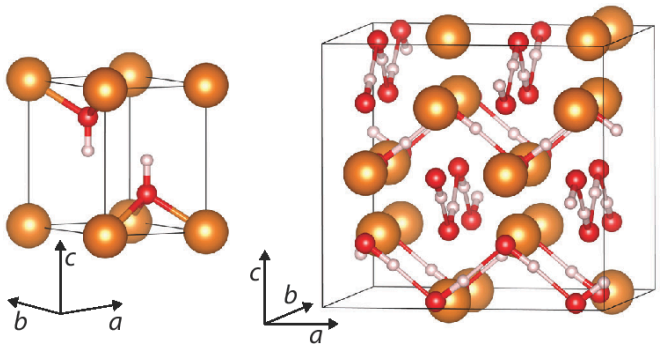

Fig. 1. (a) The low pressure phase of brucite with space group symmetry. (b) The high-pressure phase of $Mg(OH)_2$ with tetragonal space group symmetry. Both the structures are drawn to same scale at P= 20 GPa. Gold (red, white) spheres denote Mg (O, H) atoms. Hydrogen bonds in the tetragonal phase are indicated by thin lines.

helpful for experimental discoveries.(23) Here, we suggest that brucite transforms to a new high-pressure phase at conditions relevant to subducting slabs in the mantle transition zone and lower mantle, i.e. pressures of ∼20 GPa and temperatures of ∼800 K.

Results

Our density functional calculations give excellent agreement for the structural parameters of brucite ($P\bar{3}m1$) with experimental data at P=1atm, see Table 1. They also correctly reproduce the pressure-induced stabilization of hydrogen bond formation and static proton disorder, in the form of the $P\bar{3}$ phase,(16) see the upper panel of Figure 1. For those two known brucite phases, decomposition into periclase (MgO) and ice-VIII is then calculated to occur at 18 and 21 GPa, respectively, i.e. in the Earth mantle transition zone. This agrees reasonably well with thermodynamic modeling based on measured *P-V-T* equation of state for brucite, which estimated a decomposition pressure of 27 GPa at T=300K.(24) Note that brucite has been compressed significantly beyond this pressure, likely due to kinetic barriers in the decomposition reaction.(24, 25)

Our crystal structure prediction runs, however, revealed a candidate for a high-pressure phase of $Mg(OH)_2$ with tetragonal space group symmetry ($P4_12_12$), which is energetically more stable than both known modifications above 17 GPa, see the upper panel of Figure 2. With the appearance of a new high-pressure phase, the thermodynamic stability limit of $Mg(OH)_2$ (towards decomposition into MgO and ice) is shifted to significantly higher pressures: by 8 GPa in the ground state, from 21 GPa to 29 GPa. This delays the decomposition of $Mg(OH)_2$ from the lower part of the mantle transition zone (the pressure region 13-21 GPa)(26) deep into the lower mantle. The stability of the tetragonal $Mg(OH)_2$ phase is unaffected by the choice of exchange-correlation functional or the inclusion of zero-point effects (ZPE). For instance, using the vdW-DF approach with the optB88 functional,(27–30) which includes dispersion interactions based on the electronic density, instead of the PBE functional, we find tetragonal $Mg(OH)_2$ to be stable from 18 to 27 GPa. When ZPE are included with the PBE functional, tetragonal $Mg(OH)_2$ is stable from 19 to 33 GPa.

We used the quasi-harmonic approximation to estimate the Gibbs free energies of the relevant phases and construct the finite-temperature phase diagram of $Mg(OH)_2$. To that end, we included the vibrational contribution to the entropy of each phase, which results in

$$F(T,V) = E_0(V) + k_B T \int_0^\infty g(\omega) \ln\left[2\sinh\left(\frac{\hbar\omega}{2k_B T}\right)\right] d\omega$$

where $g(\omega)$ is the phonon density of states obtained from finite displacement calculations. As shown in the lower panel of Figure 2, this results in a large stability field for the tetragonal $Mg(OH)_2$ phase, up to T=800 K at 30 GPa, where it forms a triple point with brucite (in the $P\bar{3}$ model) and the decomposition into MgO + Ice-VII. This triple point corresponds to a depth of about 800 km, in the upper reaches of the lower mantle, and approaches cold geothermal gradients estimated for subducting slabs(23, 31, 32) and the melting line of ice.(33, 34) We included in this phase diagram the calculated geotherm for old and rapidly descending slabs as solid blue line.(32) This should serve as a low-temperature boundary for mantle slab geotherms (we extrapolated the data from ref. (32) beyond 20 GPa in a power expansion). We did not consider nuclear quantum effects in the construction of the phase diagram. Those can play an important role in aqueous systems(35) and might affect the phase transitions pressures in the low-temperature region – in particular if the protons' chemical environment differs significantly across the respective phases. There is some indication (see below) that the hydrogen bonds in tetragonal $Mg(OH)_2$ are stronger than in brucite.

The tetragonal $Mg(OH)_2$ phase ($P4_12_12$) is very different from the low-pressure layered phase (see Figure 1, and Table 1 for structural data). The high-pressure phase forms a three-dimensional network of edge-sharing MgO_6 octahedral units. In fact, the phase (when ignoring protons) is isostructural with the anatase-TiO_2 crystal structure, but with MgO_6 octahedral units that are less distorted compared to the TiO_6 octahedral units in anatase (see inset in lower panel of Figure 2). The protons are located in channels in between the MgO_6 polyhedral units. Alternatively, the crystal structure can be characterized by zig-zag hydrogen-bonded O-H…O-H chains running along the *a* and *b* directions, and which are lying in the *bc* and *ac* planes, respectively. In the ground state, the O-H vectors order antiferroelectrically (see Figure 1), but it is very likely that proton disorder sets in at finite temperatures. The major structural differences compared to the low-pressure phase of brucite suggest that there are significant kinetic barriers to transform from the layered phase into the tetragonal phase (just as for the decomposition), which would explain why the transition has not been observed in room-temperature experiments to pressures well into the predicted pressure stability region of the tetragonal phase.

The pressure-volume relation for brucite ($P\bar{3}$) can be described by a Birch Murnaghan equation of state with equilibrium volume $V_0^{P\bar{3}}$ = 41.68 (± 0.09) Å^3, bulk modulus $K_0^{P\bar{3}}$ = 43.4 (± 1.1) GPa, and its pressure derivative $K_0'^{P\bar{3}}$ = 5.39 (± 0.10). In contrast to brucite, the three-dimensional network of MgO_6 polyhedra in tetragonal $Mg(OH)_2$ allows for a substantially more compact packing with $V_0^{P4_12_12}$ = 38.06 (± 0.07) Å^3, $K_0^{P4_12_12}$ = 67.3 (± 1.6) GPa, and $K_0'^{P4_12_12}$ = 4.91 (± 0.09). At 1 bar the tetragonal phase is 8.67% smaller than brucite, and stiffer by ∼55%. At 20 GPa, where tetragonal $Mg(OH)_2$ has the lower enthalpy, it is 3.8% more compact than the brucite ($P\bar{3}$) phase.

Although the tetragonal phase is denser compared to the brucite phase, at 1 bar, the full elastic stiffness tensor reveals significant anisotropy. The principal stiffness components are related as $c_{11}^{P4_12_12} \sim 1.5 \times c_{33}^{P4_12_12}$, $c_{12}^{P4_12_12} \geq c_{13}^{P4_12_12}$, and the shear stiffness components are related as $c_{44}^{P4_12_12} \geq c_{66}^{P4_12_12}$ (see Figure 3). At zero pressure (i.e., 1 bar), the Hill-averaged bulk ($K_{Hill}^{P4_12_12}$) and shear ($G_{Hill}^{P4_12_12}$) moduli are 69.5 and 55.4 GPa respectively for the tetragonal $Mg(OH)_2$ phase. This is significantly stiffer than the bulk ($K_{Hill}^{P\bar{3}}$) and shear ($G_{Hill}^{P\bar{3}}$) moduli for the trigonal phase, 46.7 and 36.4 GPa.(36) The compressional (V_P) and shear (V_S) sound velocity for the tetragonal phase are also faster compared to the trigonal phase (see Figure 3).

Table 1. | Crystal structure of brucite. Optimized crystal structures of various brucite phases, from ground state DFT-PBE calculations. First row gives experimental results for the $P\bar{3}m1$ phase at P=1atm from powder neutron diffraction.(12)

Phase	Pressure	Lattice constants	Atomic positions
$P\bar{3}m1$ (Exp)	1 atm	a= b= 3.150 Å, c= 4.770 Å α= β=90□, □γ=120□	Mg(0,0,0) O(1/3, 2/3, 0.220) H(1/3, 2/3, 0.413)
$P\bar{3}m1$ (DFT)	1 atm	a= b= 3.182 Å, c= 4.801 Å α= β=90□, □γ=120□	Mg(0, 0, 0) O(1/3, 2/3, 0.217) H(1/3, 2/3, 0.419)
$P\bar{3}$	10 GPa	a= b= 5.310 Å, c= 4.383 Å α= β=90□, □γ=120□	Mg1(0, 0, 0) Mg2(1/3, 2/3, -0.018) O(-0.006, -0.336, -0.239) H(-0.070, -0.365, -0.451)
$P4_12_12$	20 GPa	a= b= 8.178 Å, c= 7.549 Å α= β= γ= 90°	Mg1(0.380, 0.380, 0) Mg2(-0.130, -0.130, 0) Mg3(-0.370, 0.120, 0.5) O1(-0.120, 0.372, 0.266) O2(0.370, -0.122, 0.266) O3(-0.122, 0.120, 0.016) O4(0.372, -0.370, 0.016) H1(-0.126, -0.477, 0.404) H2(0.381, 0.227, 0.404) H3(0.227, 0.129, 0.154) H4(-0.477, -0.378, 0.154)

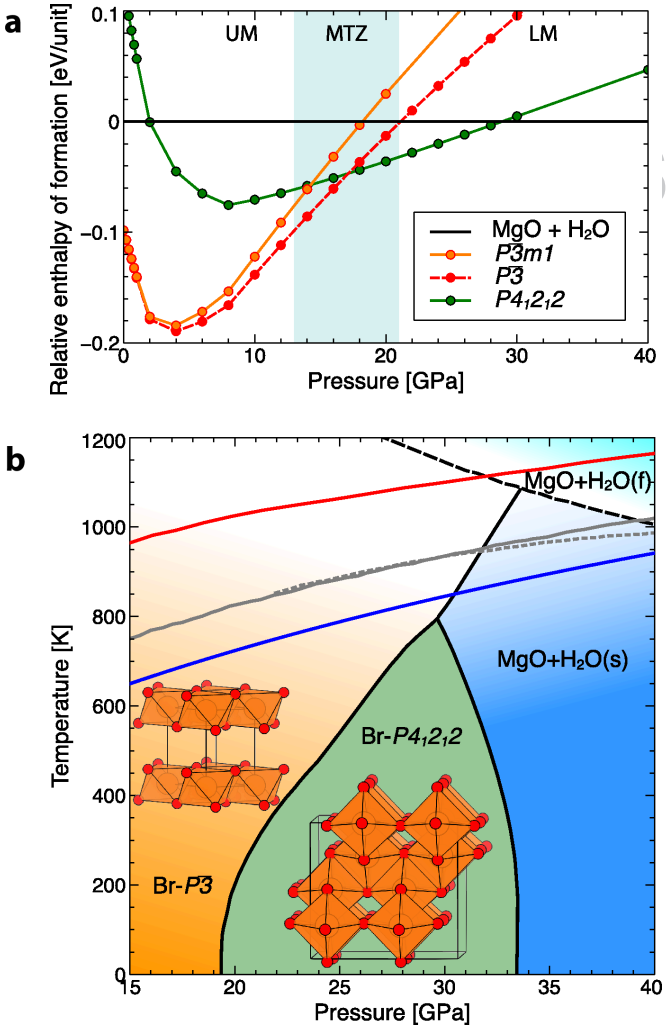

Fig. 2. Thermodynamic phase diagram of $Mg(OH)_2$.(a) Ground state enthalpies of formation of various $Mg(OH)_2$phases, relative to decomposition into MgO and ice-VIII. The light blue band represents the pressures relevant for the mantle transition zone (MTZ), upper (UM) and lower (LM) mantle. (b) Computationally derived thermodynamic phase diagram for $Mg(OH)_2$. Also shown are a parameterized high-temperature decomposition curve (dashed black line)(24), cold slab geotherms (blue and red solid lines),(23, 32) and ice melting lines (solid and dotted gray lines).(33, 34)

In addition to changes in the velocities, brucite and tetragonal $Mg(OH)_2$ have quite distinct elastic anisotropy. At low pressures (~0 GPa), the brucite phase has significant V_P-and V_S-elastic anisotropy, 57 and 46%, respectively. In comparison, tetragonal $Mg(OH)_2$ has modest V_P-and V_S-elastic anisotropies of 20 and 13% respectively (see Figure 4). At higher pressures, as the layered nature of the compound becomes less pronounced, the elastic anisotropy in brucite reduces, with V_P elastic anisotropy decreasing at a faster rate than the V_S anisotropy. In other words, the pressure derivatives of the C_{33} is greater than the pressure derivatives for the C_{11}, i.e., $dC_{11}/dP < dC_{33}/dP$. For tetragonal $Mg(OH)_2$ at higher pressure, the V_P elastic anisotropy reduces and remains fairly constant over the pressure range that corresponds to the entire upper mantle, transition zone and lower mantle. The S-wave elastic anisotropy for tetragonal $Mg(OH)_2$, on the other hand, increases almost linearly upon compression beyond 5 GPa. In this phase, the pressure derivatives of the C_{11} is slightly greater than the pressure derivatives for the C_{33}, i.e., $dC_{11}/dP > dC_{33}/dP$. In addition, even though the octahedral network in the tetragonal phase is three-dimensional, hydrogen bonds that additionally constrain the elastic response are essentially confined along the a and b directions. The predicted anisotropies could provide another diagnostic test for the presence of tetragonal $Mg(OH)_2$ in the deep mantle, but needs to be accompanied by an understanding of the rheological parameters including the slip systems, the combined elastic anisotropy and lattice preferred orientation to relate these calculated numbers to the seismic anisotropy observed in the deep mantle and in subduction zone settings.

Tetragonal $Mg(OH)_2$ is an ionic compound. A topological analysis of the electron density based on Bader's Quantum Theory of Atoms in Molecules (QTAIM)(37) suggests partial atomic charges of +1.61/-0.80 electrons for Mg^{2+} and OH^- ions respectively at 20 GPa. This is very similar to the partial charges of +1.65/-0.82 electrons in brucite ($P\bar{3}$) at the same pressure. The high-pressure phase does, however, feature stronger hydrogen bonds, as the structural rearrangement in $P4_12_12$ results in much shorter hydrogen-bonded separations: at 20 GPa, $d_{OH...O}$=1.62 Å, compared to 1.87 Å in the $P\bar{3}$ phase. As a consequence, the covalent O-H bonds are somewhat extended and arguably weakened in the $P4_12_12$ phase. At 20 GPa, the hydroxyl bond length d_{OH} is ~1.01 Å for $P4_12_12$ compared to 0.98 Å in the $P\bar{3}$ phase.

The changes in the hydrogen bonding lead to significant differences in the vibrational properties, which should make detection of the high-pressure phase quite straightforward. In Figure 5, we show calculated O-H stretch modes of the different phases as a function of $d_{O...O}$ distance, compared to an empirical functional relation established from experimental spectroscopic data on hydrous minerals.(38) Calculated frequencies for the $P\bar{3}m1$ and $P\bar{3}$ phases give, as has been noted before,(39, 40) good accounts of existing experimental data: in $P\bar{3}m1$, the O-H stretch

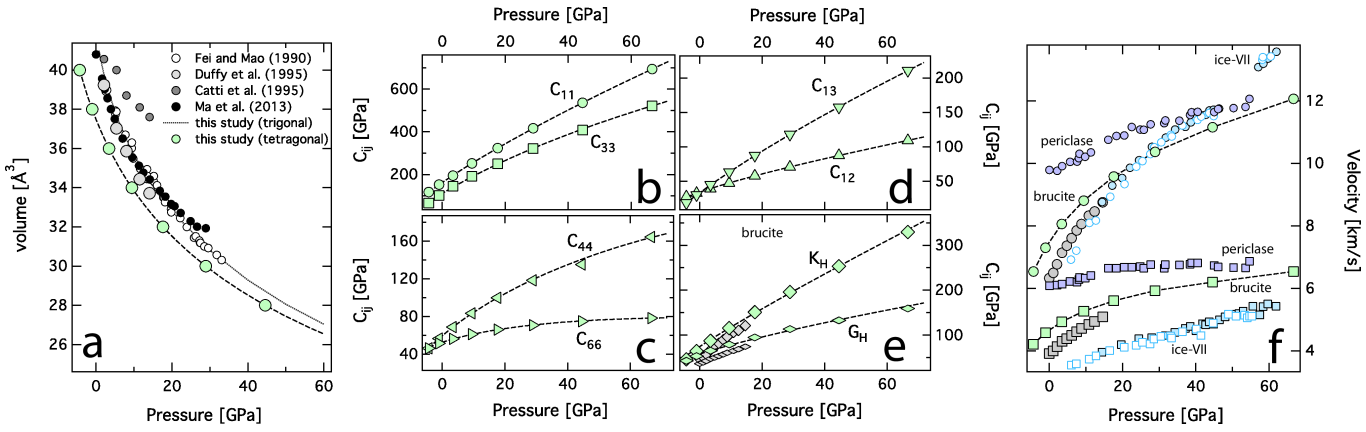

Fig. 3. Equation of state, elasticity and sound velocity of $Mg(OH)_2$.(a) Plot of volume as a function of pressure. Green symbols and thin dotted line refer to the - and -$Mg(OH)_2$phases, respectively. The dashed line gives the finite strain fit to the phase. Experimental results are shown in filled light grey (single crystal X-ray diffraction), dark grey (powder neutron diffraction), black, and white symbols (synchrotron based powder X-ray diffraction), from Refs. (12, 14, 24, 25). (b) The full elastic stiffness tensor and the Hill-averaged Bulk (K_H) and Shear (G_H) moduli for tetragonal $Mg(OH)_2$as function of pressure. (c) Calculated compressional/shear sound wave velocities (circles/squares) for tetragonal brucite (light green symbol). Grey symbols refer to the experimentally determined sound velocity of brucite.(36) Experimental data are given for the decomposition products periclase (MgO) (filled blue symbols)(63) and ice-VII (filled light blue symbols- compression, white symbols- decompression).(50)

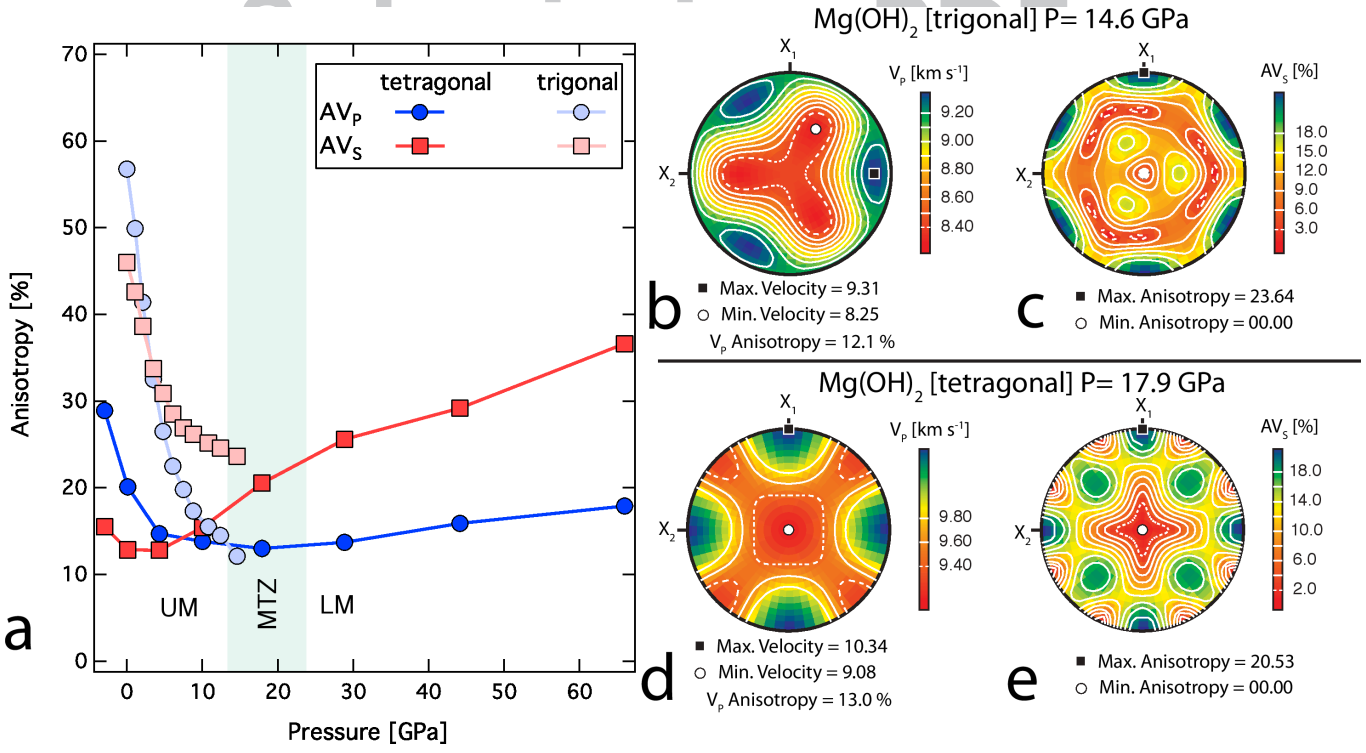

Fig. 4. Elastic anisotropy of $Mg(OH)_2$. (a) Plot of P-wave anisotropy (AV_P, blue) and S-wave anisotropy (AV_S, red) as a function of pressure. The light and dark color symbols correspond to trigonal (brucite) and tetragonal $Mg(OH)_2$, respectively. (b) and (d) show the stereographic projection of the P-wave velocity variations across the orthogonal directions for both phases. (c) and (e) shows the stereographic projection of the S-wave anisotropy variations across the orthogonal directions for both phases. The orthogonal coordinates X_1 and X_2 are shown in the stereographic projections. The X_3 axis is perpendicular to both X_1 and X_2 axes. The color shadings are in inverse logarithmic scales. The minimum and maximum velocity directions for tetragonal $Mg(OH)_2$ along the X_3 and X_1 axes coincide with the extremal C_{33} and C_{11} elastic constants, respectively.

frequency is almost independent of pressure (i.e., independent of the $d_{O...O}$ distance), whereas the $P\bar{3}$ phase reproduces the softening of the O-H stretch modes due to increased hydrogen bonding under pressure. Note that in Figure 5 we have shifted the axes of computed against experimental frequencies by 100 cm^{-1} to account for the anharmonicity of the O-H stretch.(40) The hydrogen bonding is much more pronounced in the tetragonal phase, and as a consequence its O-H stretch frequencies are significantly redshifted, about 400 cm^{-1} relative to the $P\bar{3}$ phase, and also show a more rapid decrease upon compression. At 20 GPa, where tetragonal $Mg(OH)_2$ should become stable at low temperatures, ν_{OH}=2840…3140 cm^{-1} in our calculations, while the $P\bar{3}$ phase at the same pressure has ν_{OH}=3540…3670 cm^{-1}. The stretch mode frequencies of tetragonal $Mg(OH)_2$ at low pressures (large $d_{O...O}$ distance) are significantly lower than the correlation from Ref. (38) suggests; however, under compression, in the region of its stability, the calculated modes are in quite good agreement with the empirical relation.

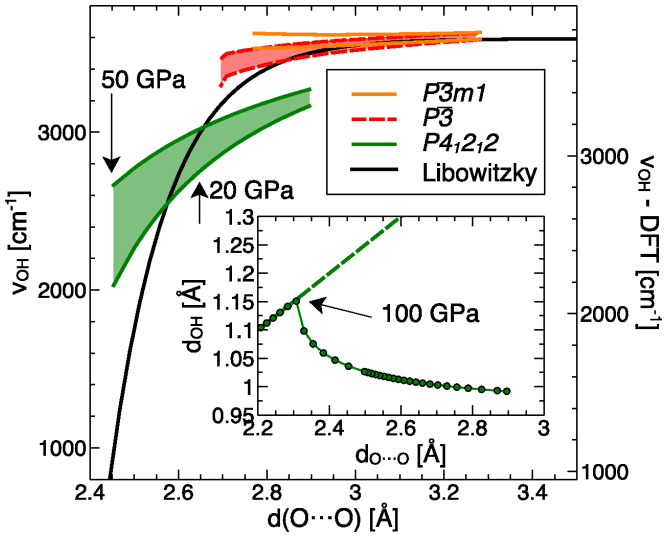

Fig. 5. Hydrogen bonding in $Mg(OH)_2$. Calculated O-H stretch frequencies in the low- and high-pressure phases of $Mg(OH)_2$, as function of hydrogen-bonded distance $d_{O...O}$. Also shown is a correlation curve based on ambient pressure data for various hydrous phases including minerals.(38) The red and green shaded region indicates the complete range of modes for the and phases respectively. The inset shows a plot of d_{OH} vs $d_{O...O}$ for tetragonal $Mg(OH)_2$. The hydrogen bond symmetrization (d_{OH}=1/2$d_{O...O}$) occurs at 100 GPa. Note calculated frequencies are red-shifted by 100 cm^{-1} with respect to the functional fit.

In the inset of Figure 5, we visualize the relation between $d_{O...O}$ and the covalent bond length d_{OH} for tetragonal $Mg(OH)_2$. We find that hydrogen bond symmetrization occurs around 100 GPa, which is much higher than in the hydrous phases δ-AlOOH, phase D ($MgSi_2O_4(OH)_2$) and phase H ($MgSiO_4H_2$), where symmetrization is seen around 30-40 GPa.(41–43) While nuclear quantum effects can significantly reduce the symmetrization pressure (in ice, for instance, from ∼100 to 65 GPa),(44, 45) we do not expect tetragonal $Mg(OH)_2$ to feature symmetric hydrogen bonds in its region of thermodynamic stability.

Discussion

Our first-principles calculations suggest that upon compression, the hydrous mineral brucite will transform to a dense phase with a three-dimensional network structure, before eventual decomposition into periclase (MgO) and ice-VII (H_2O). The new phase is found to be stable at pressure-temperature conditions that correspond to cold subducting slabs in Earth's mantle transition zone and lower mantle. It is possible that configurational disorder, on the proton and/or cation sites (for instance by forming (Mg, Fe, Ca)$(OH)_2$), stabilizes tetragonal $Mg(OH)_2$ at higher temperatures. It is also known that brucite and gibbsite ($Al(OH)_3$) have similar structures and can form mixed layered double hydroxides.(46) A high-pressure phase of gibbsite exists, δ-$Al(OH)_3$, that comprises a three-dimensional structure of corner-sharing AlO_6 octahedra.(47, 48) It is thus conceivable that elevated temperatures stabilize a high-pressure solid solution $(Mg_{1-x}Al_x)(OH)_{2+x}$ with a more complex three-dimensional network structure, or a tetragonal structure $[(Mg_{1-x}Al_x)(OH)_2]^{x+}$ balanced by an appropriate anion presence, e.g. $(A^-)_x$. Any incorporation of Al^{3+} in high-pressure $Mg(OH)_2$ is also likely to enhance its thermal stability: recent studies on aluminium incorporation in phase-D ($Al_2SiO_4(OH)_2$) have shown that it enhances its thermal stability significantly.(49) Thus, dense tetragonal $Mg(OH)_2$ together with other dense hydrous phases could act as an efficient carrier of water in cold subduction slabs. The emergence of this new, more stable compound at the edge of the MgO-H_2O-SiO_2 phase diagram has implications for the relative stability of more complex MSH phases at similar conditions.

We find that the tetragonal $Mg(OH)_2$ phase follows conventional high-pressure paradigms in that a layered structure is replaced by a more compact three-dimensional structure upon compression – the unexpected result is that this transition occurs (consistently in our calculations) *before* the decomposition reaction becomes favorable. Besides being more compact, the new phase is significantly stiffer than known brucite, which could lead to characteristic seismic signatures. A transition from the trigonal to the tetragonal phase is likely to be marked by an enhancement in both P and S-wave velocity. Under further compression, as tetragonal $Mg(OH)_2$ decomposes to a mixture of MgO and H_2O (ice) around 30 GPa, the P-wave velocity is likely to enhance whereas the S-wave velocity is likely to decrease, owing to significantly lower S-wave velocity for ice-VII at high pressure.(50) In combination (see Figure 3), both effects provide for a distinct test of the presence for the denser tetragonal phase of $Mg(OH)_2$ in cold subduction zones. However, it is very likely that the magnitude of the velocity discontinuity owing to the dissociation of tetragonal $Mg(OH)_2$ might be smeared by the presence of additional chemical components, which in turn is likely to stabilize other hydrous phases.

Tetragonal $Mg(OH)_2$ also features significantly stronger hydrogen bonds and weaker covalently bound hydroxyl groups compared to the trigonal phase, which we predict to lead to a very different spectroscopic signature, and could also result in qualitatively different proton diffusion behavior at elevated temperatures. The weaker covalent O-H bonds are likely to reduce the temperature where proton diffusivity sets in, and further stabilize the tetragonal phase over the trigonal phase at high temperature. On the other hand, due to the anatase-like structure of tetragonal $Mg(OH)_2$, protons can diffuse along one-dimensional channels of the MgO_6 polyhedral network, whereas in the low-pressure trigonal phase they can diffuse in two-dimensional wells between MgO_6 sheets. This is likely to significantly influence proton-induced electrical conductivity of the high-pressure phase of $Mg(OH)_2$. At the base of the mantle transition zone, several thermodynamic processes occur that might induce partial melting, as documented in seismological observations.(2, 51) First, the dissociation of high-pressure $Mg(OH)_2$ and other dense hydrous magnesium silicates such as phase-H(23) and phase-D(52) release water, which is likely to reduce the solidus of the lower mantle and lead to partial melting. In addition, it is known that there is a drastic reduction in the water storage capacity between the mantle transition zone minerals and lower mantle minerals, which also helps in reduction of the lower mantle solidus and thus helps in initiating partial melting in the lower mantle. Both processes may occur simultaneously and need to be understood to gain detailed insight into the deep Earth water budget.

Methods

We performed density functional theory calculations in conjunction with the projector augmented wave (PAW) method and plane wave basis sets as implemented in the Vienna Ab initio Simulation Package.(53–55) Plane wave cutoffs of E_c= 800 eV and k-point sampling densities of 20/Å^{-1} were found to give sufficiently converged energies and forces. Electronic exchange-correlation energies are approximated with the PBE generalized gradient functional,(56) and geometries were optimized until remaining forces on the atoms were smaller than 1 meV/Å.

Crystal structure predictions were then run at 20, 50 and 100 GPa, with two and four formula units per unit cell, and utilizing approaches based on evolutionary algorithms and the particle swarm optimization method as implemented in the XtalOpt and CALYPSO packages.(57, 58) Around 600 structures were optimized in each search run. Phonon dispersions and densities of state were obtained with the finite displacement method using the PHON program and appropriate supercells of the relevant structures, with central difference displacements of ±0.02Å and up to 640 atoms.(59)

We applied ±1% strains to accurately determine the stresses in the limit of small strain.(60) The elastic constants C_{ij} were obtained from the stress-strain relation, $\sigma_i = C_{ij}\varepsilon_j$ (in Voigt notation).(61) The pressure de-

pendence of the full elastic stiffness tensor was fitted with the finite strain formulation.(60) The P-wave and S-wave anisotropy are defined as $AV_P = \frac{100 \times (V_{Pmax} - V_{Pmin})}{(V_{Pmax} + V_{Pmin})/2}$ and $AV_S = \frac{100 \times (V_{Smax} - V_{Smin})}{(V_{Smax} + V_{Smin})/2}$ respectively. We used petrophysical software to determine the elastic anisotropy.(62)

Acknowledgements

A.H. wants to thank John S. Loveday for fruitful discussions. M.M. is supported by NSF grant EAR/1639552. Computational resources provided by the UK National Supercomputing Service through the UKCP consortium (funded by EPSRC Grant EP/K01465X) and project ID d56 'Planetary Interiors', by the Condensed Matter Centre for Doctoral Training (funded by EPSRC Grant EP/L015110/1), and by the Royal Society (Research Grant RG150247) are gratefully acknowledged. Supplementary research data, in compliance with EPSRC research data policy, can be accessed at http://dx.doi.org/10.748-8/ds/xxxx.

1. Pearson DG et al. (2014) Hydrous Mantle Transition Zone Indicated by Ringwoodite Included within Diamond. *Nature* 507:221–4.
2. Schmandt B, Jacobsen SD, Becker TW, Liu Z, Dueker KG (2014) Dehydration Melting at the Top of the Lower Mantle. *Science* 344:1265–8.
3. Hirschmann MM (2006) Water, Melting, and the Deep Earth H_2O Cycle. *Annu Rev Earth Planet Sci* 34:629–653.
4. Pavese A, Catti M, Ferraris G, Hull S (1997) P-V equation of state of portlandite, $Ca(OH)_2$, from powder neutron diffraction data. *Phys Chem Miner* 24:85–89.
5. Parise JB et al. (1998) Pressure dependence of hydrogen bonding in metal deuteroxides: a neutron powder diffraction study of $Mn(OD)_2$ and β-$Co(OD)_2$. *Phys Chem Miner* 25:130–137.
6. Parise JB, Loveday JS, Nelmes RJ, Kagi H (1999) Hydrogen Repulsion "Transition" in $Co(OD)_2$ at High Pressure? *Phys Rev Lett* 83:328–331.
7. Hemmingsen L et al. (1999) Structure, Chemical Bonding, and Nuclear Quadrupole Interactions of β-$Cd(OH)_2$: Experiment and First Principles Calculations. *Inorg Chem* 38:2860–2867.
8. Cairns RW, Ott E (1933) X-Ray Studies of the System Nickel—Oxygen—Water. I. Nickelous Oxide and Hydroxide1. *J Am Chem Soc* 376:527–533.
9. Lutz HD, Möller H, Schmidt M (1994) Lattice vibration spectra. Part LXXXII. Brucite-type hydroxides $M(OH)_2$ (M= Ca, Mn, Co, Fe, Cd)--IR and Raman spectra, neutron diffraction of $Fe(OH)_2$. *J Mol Struct* 328:121–132.
10. Meade C, Jeanloz R (1990) Static compression of $Ca(OH)_2$ at room temperature: Observations of amorphization and equation of state measurements to 10.7 GPa. *Geophys Res Lett* 17:1157–1160.
11. Parise JB, Leinenweber K, Weidner DJ, Tan K, Von Dreele RB (1994) Pressure-induced H bonding: Neutron diffraction study of brucite, $Mg(OD)_2$, to 9.3 GPa. *Am Mineral* 79:193–196.
12. Catti M, Ferraris G, Hull S, Pavese A (1995) Static compression and H disorder in brucite, $Mg(OH)_2$, to 11 GPa: a powder neutron diffraction study. *Phys Chem Miner* 22:200–206.
13. Kruger MB, Williams Q, Jeanloz R (1989) Vibrational spectra of $Mg(OH)_2$ and $Ca(OH)_2$ under pressure. *J Chem Phys* 91:5910–5915.
14. Duffy TS, Meade C, Yingwei Fei, Ho-Kwang Mao, Hemley RJ (1995) High-pressure phase transition in brucite, $Mg(OH)_2$. *Am Mineral* 80:222–230.
15. Raugei S, Silvestrelli P, Parrinello M (1999) Pressure-Induced Frustration and Disorder in $Mg(OH)_2$ and $Ca(OH)_2$. *Phys Rev Lett* 83:2222–2225.
16. Mookherjee M, Stixrude L (2006) High-pressure proton disorder in brucite. *Am Mineral* 91:127–134.
17. Loveday JS et al. (1996) The structure and structural pressure dependence of sodium deuteroxide-V by neutron powder diffraction. *J Phys Condens Matter* 8:L597–L604.
18. Hermann A, Ashcroft NW, Hoffmann R (2014) Lithium Hydroxide, LiOH, at Elevated Densities. *J Chem Phys* 141:024505.
19. Hermann A, Guthrie M, Nelmes RJ, Loveday JS (2015) Pressure-induced Localisation of the Hydrogen-Bond Network in KOH-VI. *J Chem Phys* 143:244706.
20. Hermann A (2016) High-pressure Phase Transitions in Rubidium and Caesium Hydroxides. *Phys Chem Chem Phys* 18:16527–16534.
21. Oganov AR, Ono S (2004) Theoretical and experimental evidence for a post-perovskite phase of $MgSiO_3$ in Earth's D" layer. *Nature* 430:445–8.
22. Tsuchiya J (2013) First principles prediction of a new high-pressure phase of dense hydrous magnesium silicates in the lower mantle. *Geophys Res Lett* 40:4570–4573.
23. Nishi M et al. (2014) Stability of Hydrous Silicate at High Pressures and Water Transport to the Deep Lower Mantle. *Nat Geosci* 7:224–227.
24. Fei Y, Mao H-K (1993) Static compression of $Mg(OH)_2$ to 78 GPa at high temperature and constraints on the equation of state of fluid H_2O. *J Geophys Res Solid Earth* 98:11875–11884.
25. Ma M, Liu W, Chen Z, Liu Z, Li B (2013) Compression and structure of brucite to 31 GPa from synchrotron X-ray diffraction and infrared spectroscopy studies. *Am Mineral* 98:33–40.
26. Dziewonski AM, Anderson DL (1981) Preliminary reference Earth model. *Phys Earth Planet Inter* 25:297–356.
27. Dion M, Rydberg H, Schröder E, Langreth DC, Lundqvist BI (2004) Van der Waals Density Functional for General Geometries. *Phys Rev Lett* 92:246401.
28. Román-Pérez G, Soler JM (2009) Efficient Implementation of a van der Waals Density Functional: Application to Double-Wall Carbon Nanotubes. *Phys Rev Lett* 103:096102.
29. Klimeš J, Bowler DR, Michaelides A (2010) Chemical accuracy for the van der Waals density functional. *J Phys Condens Matter* 22:022201.
30. Klimeš J, Bowler D, Michaelides A (2011) Van der Waals density functionals applied to solids. *Phys Rev B* 83:195131.
31. Eberle MA, Grasset O, Sotin C (2002) A numerical study of the interaction between the mantle wedge, subducting slab, and overriding plate. *Phys Earth Planet Inter* 134:191–202.
32. Bina CR, Navrotsky a (2000) Possible presence of high-pressure ice in cold subducting slabs. *Nature* 408:844–847.
33. Dubrovinskaia N, Dubrovinsky L (2003) Melting Curve of Water Studied in Externally Heated Diamond-Anvil Cell. *High Press Res* 23:307–311.
34. Goncharov AF et al. (2005) Dynamic Ionization of Water under Extreme Conditions. *Phys Rev Lett* 94:125508.
35. Ceriotti M et al. (2016) Nuclear Quantum Effects in Water and Aqueous Systems: Experiment, Theory, and Current Challenges. *Chem Rev* 116:7529–7550.
36. Jiang F, Speziale S, Duffy TS (2006) Single-crystal elasticity of brucite, $Mg(OH)_2$, to 15 GPa by Brillouin scattering. *Am Mineral* 91:1893–1900.
37. Bader RFW (1994) *Atoms in Molecules: A Quantum Theory* (Oxford University Press, Oxford, UK).
38. Libowitzky E (1999) in *Hydrogen Bond Research*, eds Schuster P, Mikenda W (Springer, Vienna), pp 103–115.
39. Hermansson K, Gajewski G, Mitev PD (2008) Pressure-induced OH frequency downshift in brucite: frequency-distance and frequency-field correlations. *J Phys Conf Ser* 117:012018.
40. Mitev PD, Gajewski G, Hermansson K (2009) Anharmonic OH vibrations in brucite: Small pressure-induced redshift in the range 0-22 GPa. *Am Mineral* 94:1687–1697.
41. Tsuchiya J, Tsuchiya T, Tsuneyuki S, Yamanaka T (2002) First principles calculation of a high-pressure hydrous phase, δ-AlOOH. *Geophys Res Lett* 29:1909.
42. Tsuchiya J, Mookherjee M (2015) Crystal structure, equation of state, and elasticity of phase H ($MgSiO_4H_2$) at Earth's lower mantle pressures. *Sci Rep* 5:15534.
43. Hushur A et al. (2011) Hydrogen bond symmetrization and equation of state of phase D. *J Geophys Res Solid Earth* 116:1–8.
44. Goncharov AF, Struzhkin V V., Mao H, Hemley RJ (1999) Raman Spectroscopy of Dense H_2O and the Transition to Symmetric Hydrogen Bonds. *Phys Rev Lett* 83:1998–2001.
45. Bronstein Y, Depondt P, Finocchi F, Saitta AM (2014) Quantum-driven phase transition in ice described via an efficient Langevin approach. *Phys Rev B* 89:214101.
46. Tongamp W, Zhang Q, Saito F (2007) Preparation of meixnerite (Mg-Al-OH) type layered double hydroxide by a mechanochemical route. *J Mater Sci* 42:9210–9215.
47. Xue X, Kanzaki M (2007) High-pressure δ-$Al(OH)_3$ and δ-AlOOH phases and isostructural hydroxides/oxyhydroxides: new structural insights from high-resolution 1H and 27Al NMR. *J Phys Chem B* 111:13156–13166.
48. Matsui M et al. (2011) The crystal structure of δ-$Al(OH)_3$: Neutron diffraction measurements and ab initio calculations. *Am Mineral* 96:854–859.
49. Pamato MG et al. (2014) Lower-mantle water reservoir implied by the extreme stability of a hydrous aluminosilicate. *Nat Geosci* 8:75–79.
50. Asahara Y, Hirose K, Ohishi Y, Hirao N, Murakami M (2010) Thermoelastic properties of ice VII and its high-pressure polymorphs: Implications for dynamics of cold slab subduction in the lower mantle. *Earth Planet Sci Lett* 299:474–482.
51. Lawrence JF, Wysession ME (2006) in *Earth's Deep Water Cycle*, eds Jacobsen SD, Van der Lee S (American Geophysical Union, Washington, DC), pp 251–261.
52. Ghosh S, Schmidt MW (2014) Melting of phase D in the lower mantle and implications for recycling and storage of H_2O in the deep mantle. *Geochim Cosmochim Acta* 145:72–88.
53. Kresse G, Furthmüller J (1996) Efficient Iterative Schemes for Ab initio Total-energy Calculations Using a Plane-wave Basis Set. *Phys Rev B* 54:11169–11186.
54. Blöchl PE (1994) Projector augmented-wave method. *Phys Rev B* 50:17953–17979.
55. Kresse G, Joubert D (1999) From ultrasoft pseudopotentials to the projector augmented-wave method. *Phys Rev B* 59:1758–1775.
56. Perdew JP, Burke K, Ernzerhof M (1996) Generalized Gradient Approximation Made Simple. *Phys Rev Lett* 77:3865–3868.
57. Lonie DC, Zurek E (2011) XtalOpt: An Open-source Evolutionary Algorithm for Crystal Structure Prediction. *Comput Phys Commun* 182:372–387.
58. Wang Y, Lv J, Zhu L, Ma Y (2012) CALYPSO: A Method for Crystal Structure Prediction. *Comput Phys Commun* 183:2063–2070.
59. Alfè D (2009) PHON: A Program to Calculate Phonons using the Small Displacement Method. *Comput Phys Commun* 180:2622–2633.
60. Karki BB, Stixrude L, Wentzcovitch RM (2001) High-Pressure Elastic Properties of Major Materials of Earth's Mantle From First Principles. *Rev Geophys* 39:507–534.
61. Nye JF (1957) *Physical Properties Of Crystals: Their Representation by Tensors and Matrices* (Oxford University Press, Oxford, UK).
62. Mainprice D (1990) A FORTRAN program to calculate seismic anisotropy from the lattice preferred orientation of minerals. *Comput Geosci* 16:385–393.
63. Zha C-S, Mao H, Hemley RJ (2000) Elasticity of MgO and a primary pressure scale to 55 GPa. *Proc Natl Acad Sci U S A* 97:13494–13499.